Geophys. J. Int. (1993) **112,** 481–496

Dynamic rupture processes on a dipping fault, and estimates of stress drop and strength excess from the results of waveform inversion

Takeshi Mikumo[1]* and Takashi Miyatake[2]

[1] *Disaster Prevention Research Institute, Kyoto University, Uji, Kyoto* 611, *Japan*
[2] *Earthquake Research Institute, University of Tokyo, Tokyo* 113, *Japan*

Accepted 1992 August 10. Received 1992 July 16; in original form 1991 December 17

SUMMARY

The dynamic rupture processes on a dipping fault in a horizontally layered medium are investigated on 3-D, spontaneous shear-crack models. The wave equations for the 3-D space are solved numerically by a finite difference method under appropriate boundary conditions. The displacement components right above and right below the dipping fault plane have been obtained by solving the boundary conditions across the fault. It was found that the final fault slip on the hanging wall side is appreciably larger than that on the foot wall side, and that their amount is quite sensitive to the fault depth and the elastic heterogeneities of the medium, particularly of the existence of low-velocity surface layers.

On the basis of the above model, the dynamic rupture process of the 1961 Kita–Mino earthquake in central Japan has been investigated with constraints of the fault parameters derived from the results of waveform inversion analysis. For this purpose, a locking fracture criterion was introduced for rupture propagation, from which a lower bound of the maximum shear stress before the rupture and hence of the strength excess has been estimated. The dynamic stress drop has also been evaluated by repeated iterations to minimize the difference between the dynamic and kinematic fault slips.

The results revealed quite heterogeneous distribution of strength excess, indicating large values near the SW section of the fault at shallow depths and in the central bottom section, in contrast to small values at mid-depths in the NE section around the rupture nucleus zone. The distribution of stress drop was also found to be heterogeneous, with the existence of high-stress drop zones in the NE, shallow and bottom sections and a low-stress drop zone at most of mid-depths except in the SW section. These results suggest that the dynamic rupture of this earthquake initiates at a small nucleus zone with low-strength excess and small-stress drop, then broke the shallower and deeper fault sections with moderate-strength excess and high-stress drop, and finally ruptured barrier zones with high-strength excess. These zones may be interpreted as weak and strong asperities and barriers, respectively.

Key words: dipping fault, dynamic rupture process, dynamic stress drop, strength excess, 3-D model.

1 INTRODUCTION

Dynamic fault rupture processes have been extensively investigated in recent years from both theoretical and observational sides. Recent waveform inversion techniques, based on kinematic dislocation models, using seismic data observed in the near and far fields have revealed complex faulting processes including non-uniform slip or moment-release distribution, and incoherent rupture propagation (Olson & Apsel 1982; Hartzell & Heaton 1983; Kikuchi & Kanamori 1982; Spudich & Frazier 1984; Fukuyama & Irikura 1986; Takeo 1987, 1988; Takeo & Mikami 1987, 1990; Beroza & Spudich 1988; Fukuyama 1991a, b). On the other hand, theoretical and numerical approaches particu-

* Now at: Centro Nacional de Prevencion de Disastres, Delfin Madrigal 665, Col. Santo Domingo, Del. Coyoácan, México 04360 D.F.

larly based on spontaneous, dynamic shear-crack models indicate that the complex rupture processes result mainly from non-uniform stress field, and heterogeneous distribution of frictional fault strengths, (e.g. Andrews 1976; Yamashita 1976; Das & Aki 1977a; Mikumo & Miyatake 1978; Miyatake 1980; Das 1981; Day 1982; Virieux & Madariaga 1982). Strongly heterogeneous faults yield episodic fault motions and irregular ruptures, radiate high-frequency seismic waves, and sometimes leave unbroken barriers which could be the source of eventual multiple shocks and aftershocks (Mikumo & Miyatake 1978, 1979). It has also been shown (Mikumo, Hirahara & Miyatake 1987), on the other hand, that the actual faulting processes are strongly affected by the heterogeneities of crustal materials around the fault zones, the presence of the free surface, the depth dependence of shear stress and fault strength, under realistic, tectonic and structural environments.

It is to be mentioned that all the above results have been obtained only for a fault in an infinite medium or for a vertical strike–slip fault in heterogeneous media. We are now interested in more realistic dynamic rupture processes of thrust-type and sometimes normal faulting earthquakes in subduction zones and even in continental lithospheres.

One of our primary purposes of the present paper is to understand the basic properties of dynamic rupture propagating on a dipping fault embedded in a heterogeneous medium, which is subjected to a uniform or depth-dependent shear stress. For the case of the 1985 Michoacan, Mexico earthquake, a 'crack-like rupture process' indicating a smoothly propagating rupture has been proposed (Yomogida 1988) to simulate the ground displacement records obtained right above the dipping fault plane. In this case, however, the distribution of the source duration times and the final displacements are only *a priori* assumed by using a 2-D crack analogy. For the case of the 1971 San Fernando, California earthquake, which had a thrust-type mechanism, the rupture process and ground motions have been simulated by applying a 3-D finite element technique (Toki & Sawada 1988). However, this approach requires an extremely long computer time, and a part of the obtained results appears to involve physically unreasonable oscillations. For these reasons, we deal here in a more straightforward way with the present problems as a complete 3-D spontaneous, dynamic shear crack.

Another main purpose here is to estimate the distribution of dynamic stress drop and relative peak strength over the dipping fault from the results of waveform inversion for actual earthquakes. A few attempts have been made to simulate the kinematic inversion results by comparing with the results from a number of dynamic rupture processes (Mikumo *et al.* 1987; Quin 1990). Recently, Miyatake (1992) and Fukuyama & Mikumo (1992) presented a more direct approach to infer the distribution of the dynamic parameters with constraints of the kinematic parameters such as the slip and rupture times, although these studies are for strike–slip faults.

Our final goal is to obtain detailed information about the heterogeneities of tectonic shear stress and fault strength or the possible existence of barriers and asperities in subduction zones and in continental crusts. In the present study, we are studying the dynamic rupture process of the 1961 Kita–Mino earthquake that occurred in central Honshu, Japan, which is one of tectonically most active regions.

2 MODEL AND FORMULATIONS

Now, we describe a dynamic rupture propagating over a dipping fault embedded in a horizontally layered half-space. Fig. 1 shows the geometry of the dipping fault plane located in a 3-D space. We take the xz-plane in the free surface, with the x- and z-axes being parallel and perpendicular to the direction of the fault length, and the y-axis vertically downward. The y'- and z'-axes are taken parallel and perpendicular to the dipping fault plane, respectively. Suppose that the fault has a static frictional strength σ_s, and is initially subjected to the shear stress σ_0 working parallel to the y'-axis, where σ_0 is uniform or depth-dependent, and that all these quantities are functions of position on the fault. For preliminary calculations, we assume that if σ_0 exceeds σ_s at any point on the fault, then fault slip immediately occurs there. This implies that we actually use a simple critical stress fracture criterion, which is approximately equivalent to the Irwin's criterion based on the critical intensity factor (Das & Aki 1977a). All three displacement components and six stress components at any point within our model space, which are caused by the fault slip, should satisfy the equations of motion, and hence we have the wave equations. Lame's elastic constants λ and μ and the density ρ involved in the equations are functions of depth in the present case. The wave equations can be discretized for all grid points located above and below the dipping fault plane such as given in Fig. 1, and solved by a finite difference scheme under the fracture criterion mentioned above and sets of boundary conditions.

The boundary conditions are imposed here for four different cases. Fig. 2 schematically illustrates a side view of our model space. The first set of boundary conditions on the free surface at $y = 0$ requires that the normal stress σ_{yy} and two tangential stresses σ_{yx} and σ_{yz} be zero. [Eq. (3) in Mikumo *et al.* (1987)]. The second set of boundary conditions that should be satisfied at each of the horizontal-layer interfaces included in the medium is the continuity of normal stress σ_{yy} and trangential stresses σ_{yx} and σ_{xy} and three displacement components u, v and w [Eq. (4) in Mikumo *et al.* (1987)]. The third set of boundary conditions we applied here is an absorbing boundary condition which attenuates elastic waves reflected back from artificial side and bottom boundaries of the model space. In the present case we introduce a dissipation term proportional to the particle velocity, $p\,\partial U(u, v, w)/\partial t$ into the wave equations, in a zone adjacent to the outer boundaries (Levander 1985), where p is a small dissipation coefficient.

The most important boundary conditions in the present case are those on the fault plane at $z' = 0$. The first one is $\sigma_{y'z'} = \sigma_0 - \sigma_d$, because once fault slip initiates at any point, the slip motion is resisted by the sliding frictional stress σ_d, and hence the applied stress is assumed to drop immediately to the level of σ_d. σ_d could be rate- and state-dependent as suggested from recent laboratory experiments (e.g. Dieterich 1981; Ruina 1983), but it is assumed for simplicity to be constant in the present case. Since the tangential stress $\sigma_{z'x'}$

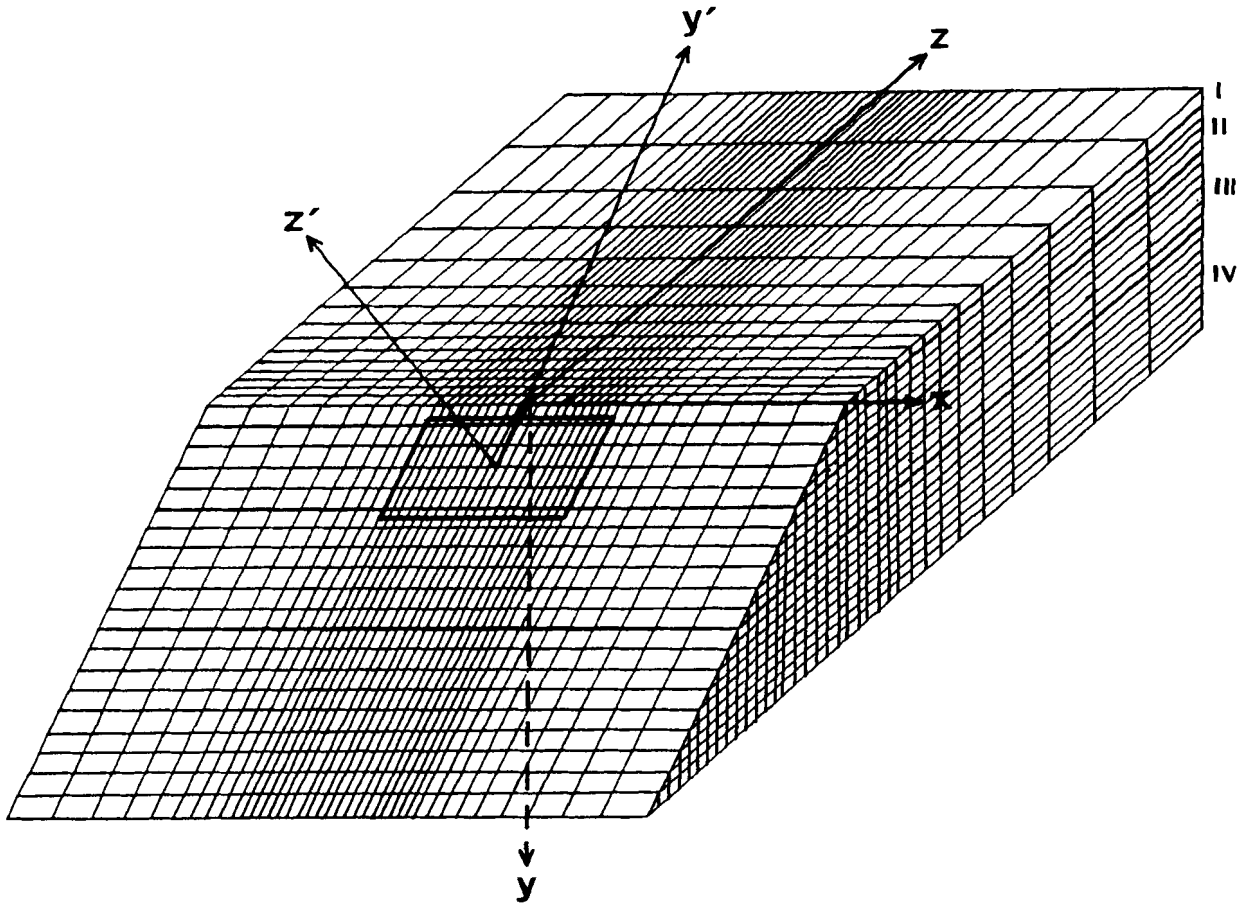

Figure 1. A schematic view of the 3-D model space and the geometry of the fault plane dealt with in this study.

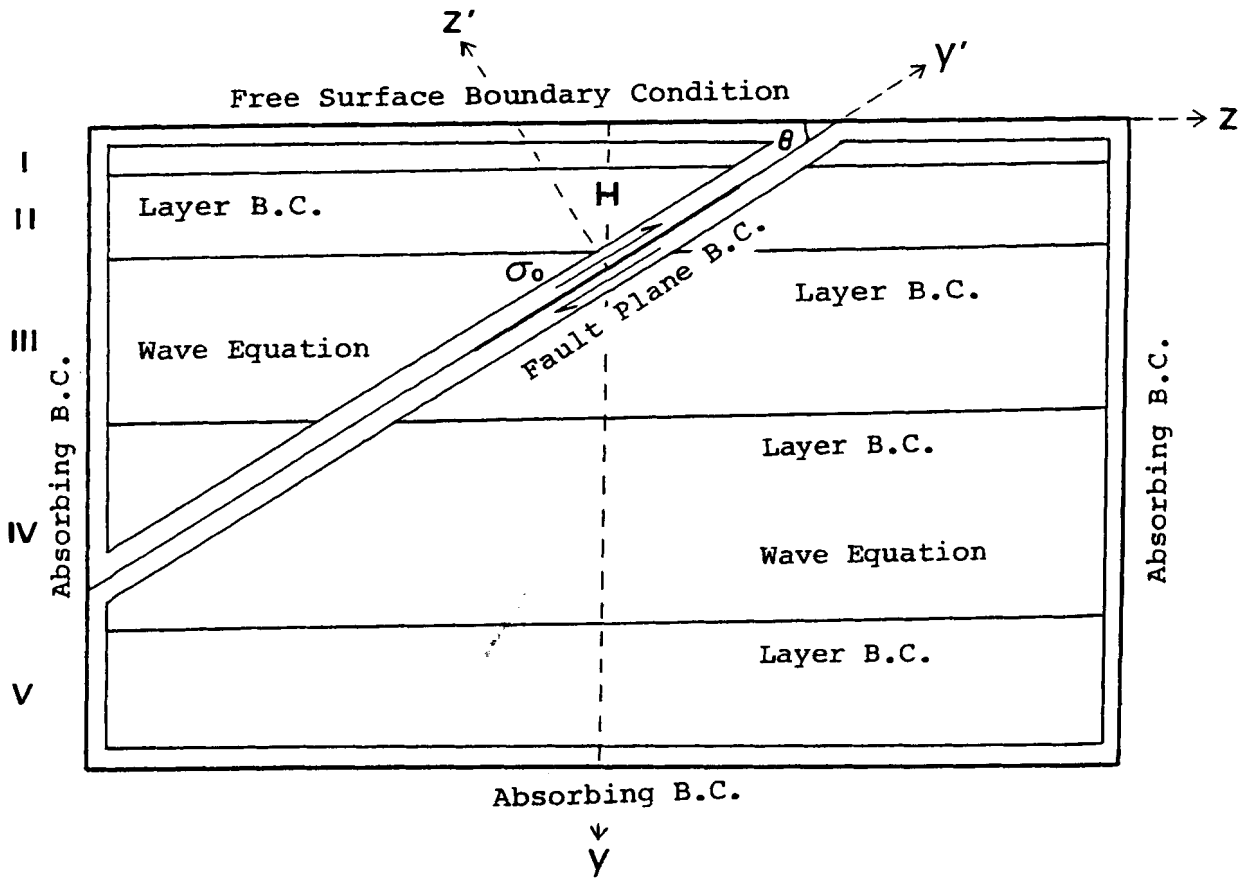

Figure 2. A side view of the model space, indicating the locations of the fault plane, free surface, layer interfaces, and the outer boundaries for which the boundary conditions are applied.

and normal stress $\sigma_{z'z'}$ should be continuous across the fault plane, we have,

$$\sigma_{x'z'} = \mu\left(\frac{\partial u'}{\partial z'} + \frac{\partial w'}{\partial x'}\right) = \text{continuous}$$

$$\sigma_{y'z'} = \mu\left(\frac{\partial v'}{\partial z'} + \frac{\partial w'}{\partial y'}\right) = \sigma_0 - \sigma_d \qquad (1)$$

$$\sigma_{z'z'} = \lambda\left(\frac{\partial u'}{\partial x'} + \frac{\partial v'}{\partial y'} + \frac{\partial w'}{\partial z'}\right) + 2\mu\frac{\partial w'}{\partial z'} = \text{continuous}.$$

Beside these, we also have the condition of continuity for the displacement component perpendicular to the fault plane,

$$w' = \text{continuous} \qquad (2)$$

since no discrepancy occurs in the normal component across the fault. If we use subscripts 1 and 2 indicating the stress and displacement components right above and right below the fault plane, respectively, as $z' \to 0$, eqs (1) and (2) can be rewritten more explicitly as,

$$(\sigma_{y'z'})_1 = \sigma_0 - \sigma_d \qquad \text{(a)}$$

$$(\sigma_{y'z'})_2 = \sigma_0 - \sigma_d \qquad \text{(b)}$$

$$(\sigma_{z'z'})_1 = (\sigma_{z'z'})_2 \qquad \text{(c)} \quad (3)$$

$$w_1' = w_2' \qquad \text{(d)}$$

$$(\sigma_{z'x'})_1 = (\sigma_{z'x'})_2. \qquad \text{(e)}$$

The boundary conditions given in eq. (3) can be discretized into the finite difference equations. Six displacement components v_1, w_1, u_1, v_2, w_2 and u_2 right above and right below at any point on the fault plane can be solved from the equations, assuming that $u_1 = u_2$ for pure thrust or normal faulting, as described in the Appendix.

3 MODEL PARAMETERS AND PRELIMINARY CALCULATIONS

For numerical calculations, the model space shown in Fig. 1 has to be taken as large as possible, even though we apply an absorbing boundary condition to the zone near the outer boundaries. The grid spacing and the time increment also have to be taken so as to satisfy the stability condition for 3-D wave propagation. In the present case, the grid spacing inside and near the fault plane in the x'- and y'- directions are chosen as $\Delta x' = \Delta y' = \Delta h$, and those in the y- and z-directions as $\Delta y = \Delta h \sin\theta$ and $\Delta z = \Delta h \cos\theta$. For $\theta = 45°$, we take $\Delta h = 1.2$ km, which gives $\Delta y = \Delta z = 0.85$ km. The fault dimension in this case is taken to be 16.8 km × 12.0 km. These grid spacings are taken to increase successively by a factor of 1.15 outside the specified zone, and the dimension of the model space here reaches 112 km, 68 km and 137 km in the x-, y-, and z-directions, respectively. The total number of grid points amounts to 92 455. The time increment is taken here as 0.05 s, and the total time steps of 300 covers 15 s after the initiation of the rupture process.

We have made a number of preliminary calculations of the dynamic rupture process for different cases. The structures incorporated in these calculations are; (1) the horizontally layered structure appropriate to a region in central Honshu, Japan (Mikumo *et al.* 1987), and (2) a homogeneous half-space with the elastic properties corresponding to those in Layer 3 in the above structure. The calculations have been made for different depths H to the centre of the fault plane varying from 6 km to 12 km, and for two different fault dips of 30° and 45°, to examine the effects of the free surface and the depth. For $H = 6$ km, the shallower edge of the fault breaks the ground surface. For the preliminary calculations, we simply assume that the static frictional strength $\sigma_s = 20.15$ MPa, sliding frictional stress $\sigma_d = 18.0$ MPa and the initial stress $\sigma_o = 20.0$ MPa, all of which are uniformly distributed over the fault plane, taking into account some experimental data $\sigma_d/\sigma_s = 0.70$–0.80 (Byerlee 1978). In this case, the expected stress drop is 2 MPa everywhere on the fault plane, and $S = (\sigma_s - \sigma_0)/(\sigma_0 - \sigma_d) = 0.1$. The detailed results from these calculations for the rupture process, the source time functions and ground displacements will be presented elsewhere (Mikumo 1992), but some of them are summarized here.

The results indicate that the rupture processes are appreciably affected by the depth to the dipping fault as well as by heterogeneous elastic properties of the medium. The amount of the final fault displacements is quite sensitive to the fault depth, indicating a rapid increase with decreasing depth, which suggests strong effects of the free surface on the dynamic rupture. These effects may be due to seismic waves radiated upward from the dipping fault and reflected back from the free surface, which could strongly enhance the shear stress on the fault. The existence of low-velocity surface layers also yields large fault displacements in a shallow section of the crust, as in the case of a vertical fault.

4 RUPTURE PROCESS OF THE 1961 KITA-MINO EARTHQUAKE

Now, we simulate the dynamic rupture process of an actual earthquake by applying the 3-D spontaneous, dynamic shear crack propagating over a dipping fault embedded in a heterogeneous medium. An example of the earthquakes taken here is the 1961 Kita–Mino earthquake that occurred in central Japan. The faulting process of this earthquake has been investigated from the observed seismic and geodetic data, including the fault–plane solution, spatial distribution of aftershocks, static vertical displacements across the epicentral area and the long-period seismograms recorded at a seismograph station 170 km away from the epicentre (Kawasaki 1975). The data indicate that this earthquake was caused by thrust faulting with right-lateral strike–slip component on a dipping fault with a northwestward dip of 60° and dimensions of 12 km × 10 km, over which the rupture propagated unilaterally southwestwards with a velocity of 3.0 km s^{-1} and a rise time of 2 s (Kawasaki 1975). The estimated average dislocation and seismic moment are 2.5 m and 9×10^{25} dyne · cm, respectively. The spatial extent of the fault zone has later been estimated as 16 km × 12 km from detailed relocation of these aftershocks (Hamada 1984). Takeo & Mikami (1990) investigated the detailed rupture process of this earthquake from waveform-inversion analysis by using the displacement-type strong motion seismograms recorded at six stations around the source region. Their estimate of the average slip and seismic moment are 0.9 m and 5×10^{25} dyne · cm, respectively, both

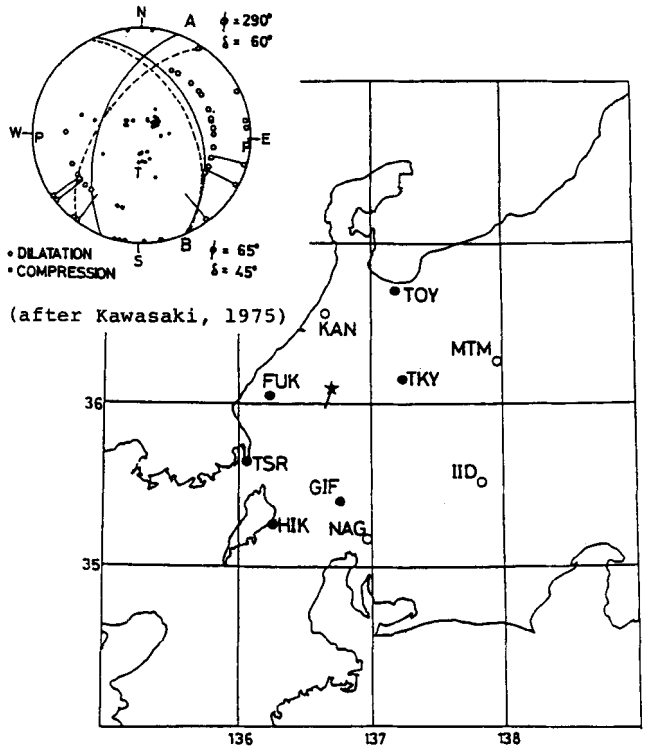

Figure 3. Locations of the 1961 Kita–Mino earthquake and the JMA stations equipped with strong motion seismographs. The top left shows the fault plane solution of this earthquake (Kawasaki 1975).

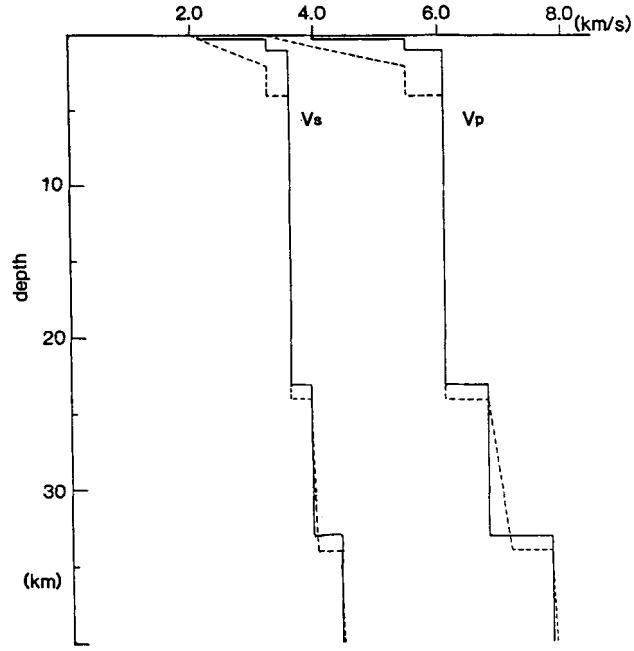

Figure 4. The horizontally layered structure adopted in this study. *Vp*: *P*-wave velocity, *Vs*: *S*-wave velocity.

of which are somewhat smaller than those estimated by Kawasaki (1975).

Fig. 3 shows the locations of the 1961 Kita–Mino earthquake and of JMA stations equipped with strong motion seismographs around the source, and also the fault plane solution of this earthquake.

4.1 Initial model

As a first step, we calculate the initial model of the dynamic rupture process of this earthquake on a thrust fault with the above dimension. In the present case, however, we assume, for simplicity, pure thrust faulting, omitting a small strike–slip component, and take a dip of 45°, since the fault plane solution obtained before may have made some allowance for the fault geometry. This slight simplification would not have serious effects on the dynamic rupture process. We also assume here that the upper edge of the fault is located at a depth of 1.7 km, since no surface fault breaks have been detected at the time of this earthquake. The depth to the centre of the fault plane is 7 km. The horizontally layered structure in the source region (Takeo & Mikami 1990) is shown in Fig. 4, but the uppermost thin surface layer has been omitted in this study. The parameters specifying the structure are given in Table 1.

As mentioned before, all dynamic rupture processes are governed by the dynamic stress drop and strength excess. However, since we do not know accurate values of the fault strength, sliding frictional stress and initial tectonic stress at this moment, we have to tentatively assign their initial estimates within a plausible range, as assumed in the preliminary calculations. These values provide only an initial reference level of fault slip and rupture velocity, and would not affect the final results.

Fig. 5 shows a perspective view of the temporal pattern of rupture propagation and fault slips right above and right below the fault plane. It should be remarked here that the fault slips on the hanging wall side V_1' are appreciably larger than those on the foot wall side V_2'. This is indeed the case for a dipping thrust or normal fault embedded in the structure with a free surface. The difference comes from the conservation of linear momentum of two blocks above and below the fault plane. This may be understood if we consider that since a smaller mass of the hanging wall block participates in the thrusting motion as compared with a larger effective mass of the foot wall block, the hanging wall velocity must be greater than the oppositely directed foot wall velocity.

The displacement source time functions at the initiation point of rupture (O) and at several selected sites on the fault plane (A–G) are shown in Fig. 6, where thick and broken curves indicate the displacement components V_1' and V_2', respectively. It can be seen that the difference between the two components is larger at shallower sites than that at

Table 1. Crustal structure appropriate to the source region in central Honshu, Japan.

No.	*Vp* (km s^{-1})	Vs (km s^{-1})	ρ(gr cm^{-3})	Depth (km)
1	5.50	3.25	2.65	4
2	6.11	3.61	2.74	21
3	6.80	3.90	2.90	6
4	7.15	4.01	3.90	5
5	7.80	4.41	3.32	

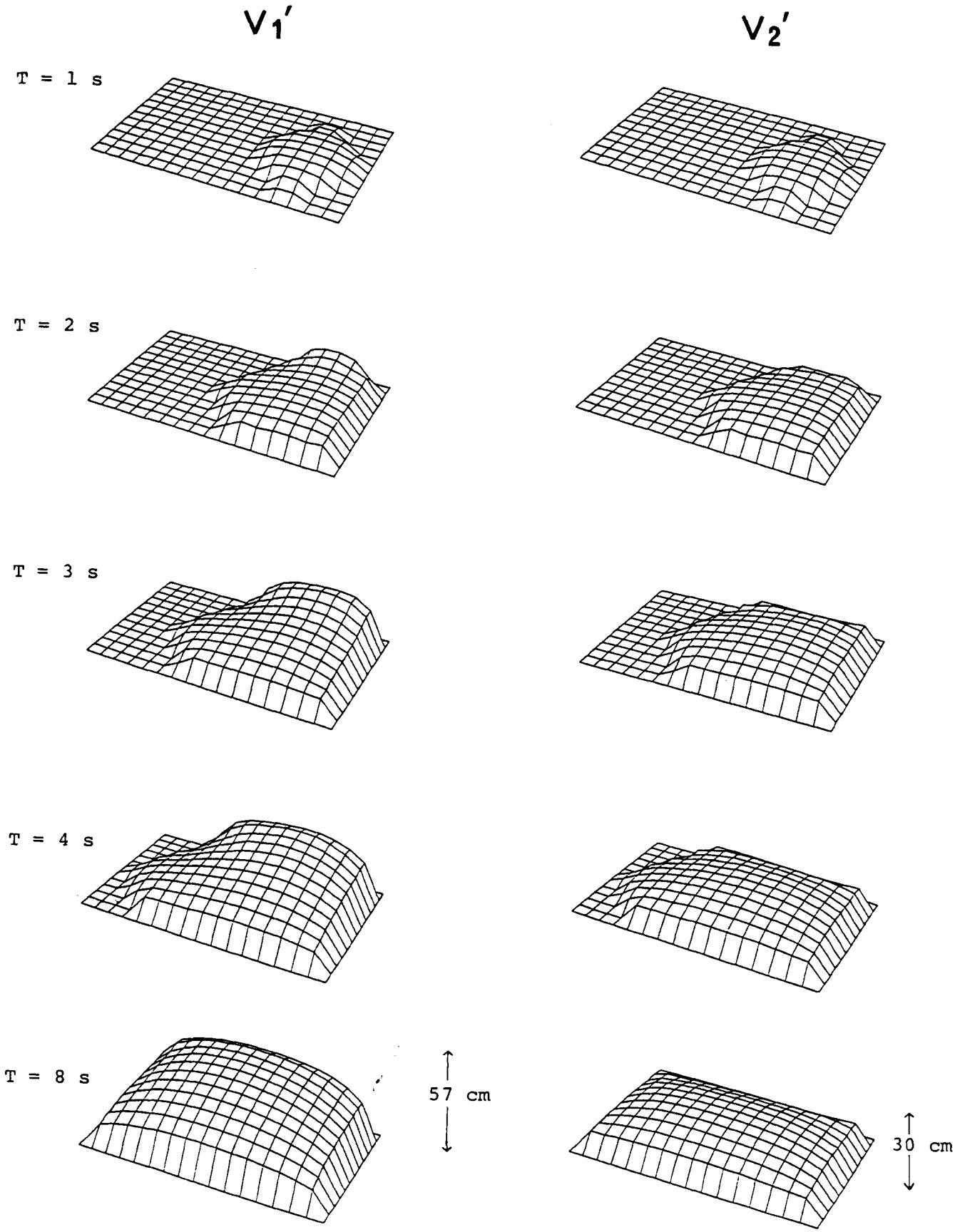

Figure 5. Temporal patterns of rupture propagation and fault slip for the initial dynamic model. V_1' and V_2' are the fault slips right above and right below the fault plane, respectively. The rupture starts from the initiation point corresponding to the location of the hypocentre of this earthquake.

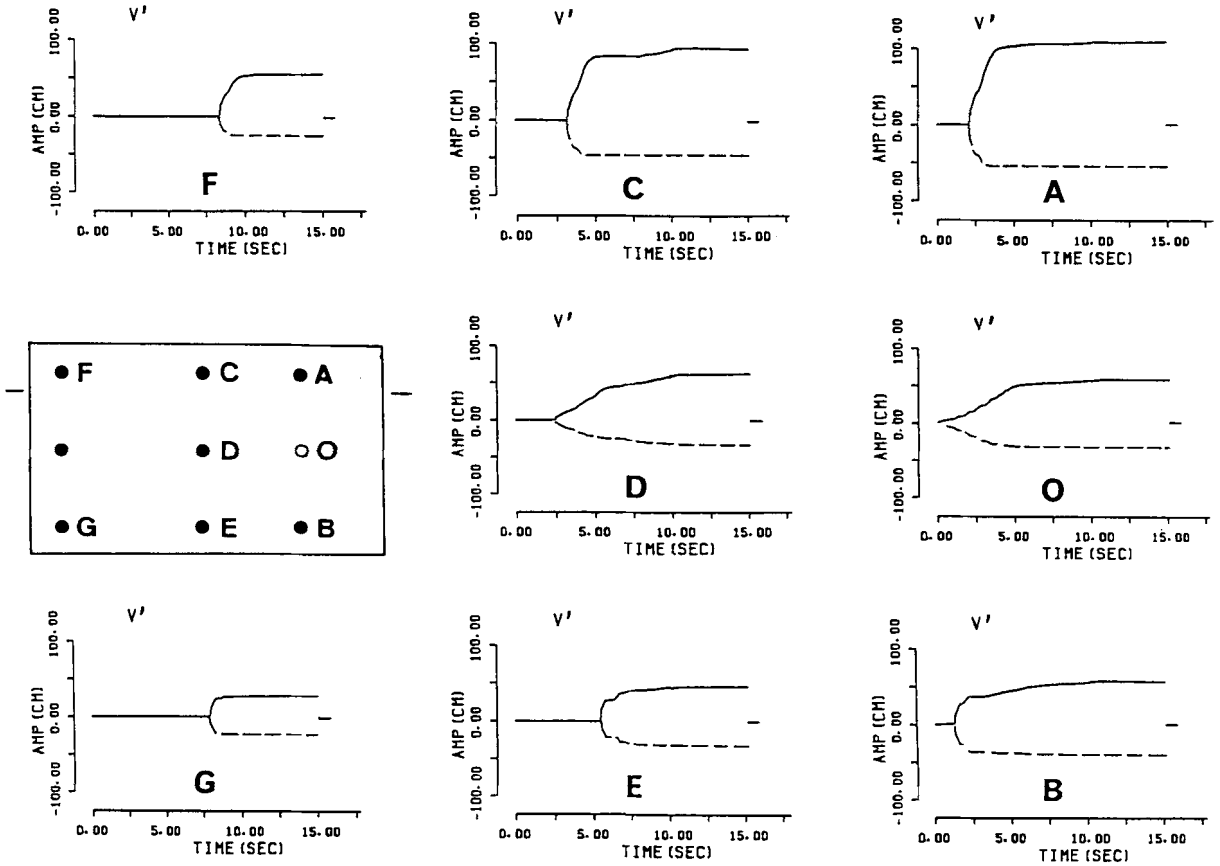

Figure 6. The displacement source–time functions at the initiation point of rupture (O) and at several selected sites on the fault plane (A–G). Solid and broken curves indicate the displacement components V_1' and V_2' parallel to the fault.

deeper sites. The larger displacements near the ground surface (A, C and F) can be accounted for by the effects of the free surface and the existence of a low-velocity surface layer, as we have mentioned in Section 3. The rise time of the source time function near the left edge of the fault plane is much shorter than that near the central portion. Fig. 7 illustrates the corresponding, temporal pattern of the total slip V_1'–V_2', which should be compared with observations. It is found that a uniform stress drop of 2 MPa assumed here yields the maximum final fault slip of 83 cm, which appears considerably smaller than those estimated from the observations.

4.2 Fitting to the results of kinematic waveform inversion

The results of waveform inversion analysis made by Takeo & Mikami (1990) are reproduced in Fig. 8. The fault plane was divided into 12 subfaults with unit dimensions of 4 km × 4 km. The right-hand side shows the rupture times at each subfault and their smoothed rupture fronts at every 1 s. This pattern indicates that the rupture starting from the northeastern end of the fault propagated southwestwards smoothly up to about 3 s, but was somewhat decelerated between 3 and 6 s around the centre bottom of the fault and after 5 s in the shallower section near the southwestern edge. On the other hand, the left-hand side shows the distribution of slip at each subfault, indicating large slip exceeding 1.5 m in the northeastern shallower section and small slip less than 0.7 m in the southwestern, shallower and deeper sections. Fig. 9 provides a comparison between the strong motion records obtained at the six stations and the corresponding synthetic seismograms calculated from the inversion results (Takeo & Mikami 1990), showing good agreement in their waveforms.

Now we are studying the actual dynamic rupture process of this earthquake, with constraints of the above kinematic fault parameters. The present problem is to derive the distribution of dynamic stress drop $\sigma_o - \sigma_d$ and strength excess $\sigma_s - \sigma_0$ over the fault, from the distribution of fault slips and rupture times obtained from the waveform inversion. The approach taken here includes two steps.

(1) We introduce a locking fracture criterion for dynamic rupture propagation, instead of using the conventional critical stress criterion employed in the initial model. The rupture at each fault segment remains locked until the rupture time t_r obtained by smoothing from the kinematic inversion, i.e. $V_1' = V_2' = 0$ for $t < t_r$. The tectonic shear stress at this segment increases as $\sigma_0 \rightarrow \sigma_0 + \delta\sigma$ as $t \rightarrow t_r$, and then drops to the level of σ_d at $t = t_r$. The peak shear strength σ_s there can be estimated from the maximum stress just before the segment breaks. The strength excess is defined here as the difference between the estimated peak strength and the assigned initial tectonic stress. This procedure is essentially the same as in Miyatake (1992), and in a sense similar to that by Quin (1990). It should be mentioned, however, that if we allow about half a second

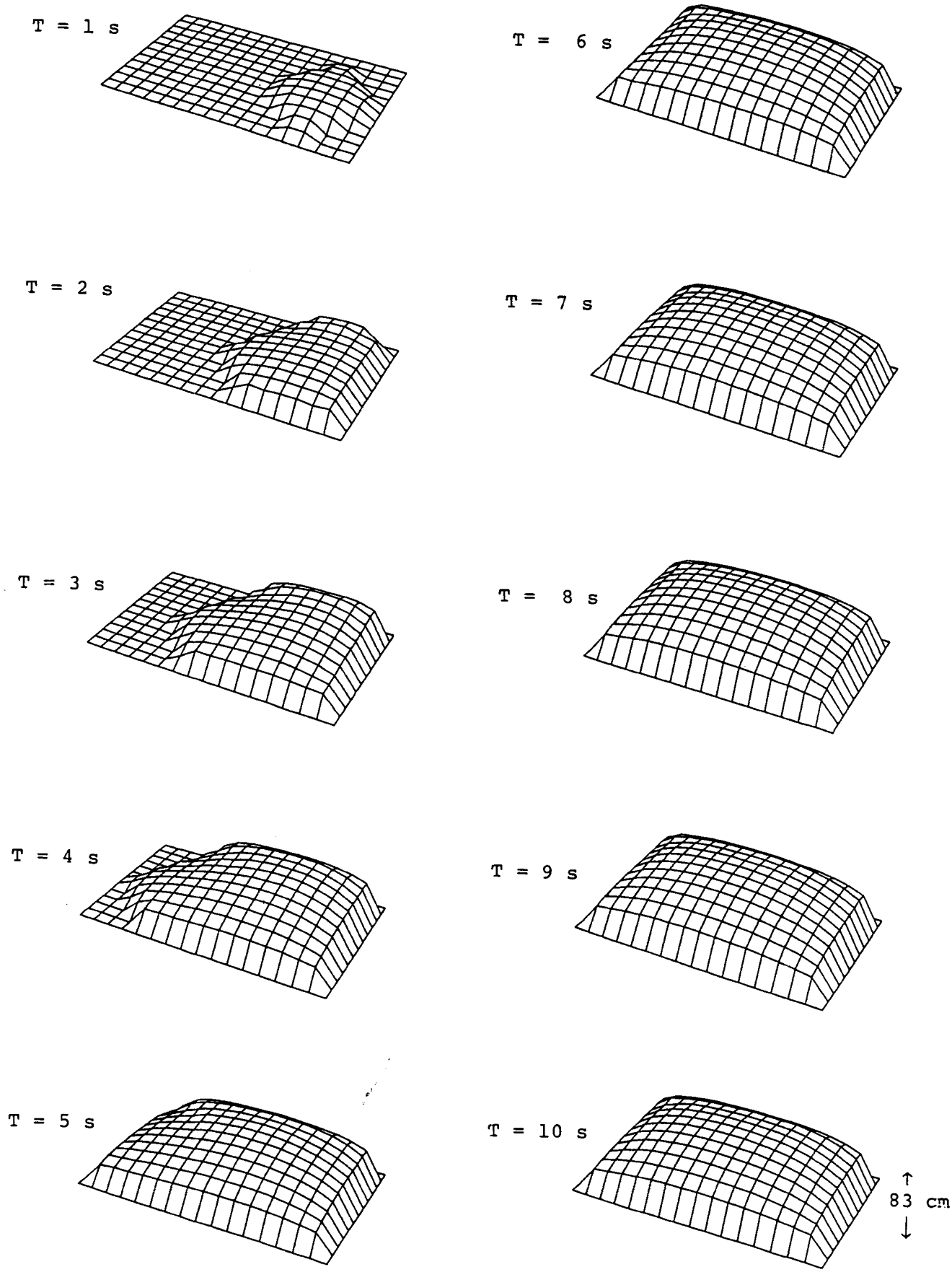

Figure 7. Temporal patterns of rupture propagation and total fault slips V_1'–V_2' for the initial dynamic model.

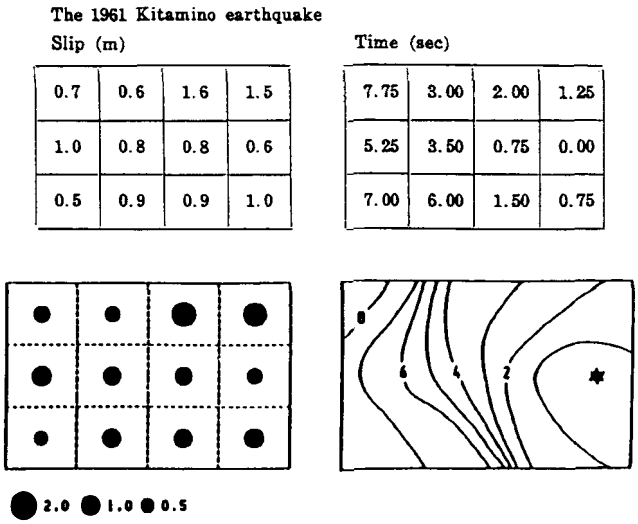

Figure 8. Distribution of the fault displacements (left-hand side) and the rupture times (right-hand side) for the 1961 Kita–Mino earthquake, which were derived from the waveform inversion of strong motion records (after Takeo & Mikami 1990).

for the discrepancy between the dynamic and kinematic rupture times as in Quin, the estimated maximum stress would give a value considerably different from its real one. Since the maximum stress and hence the peak strength estimated in this way are dependent of the grid spacing used in the numerical calculations, this should be regarded as a lower bound of its real value, as discussed in more detail in Section 5 (2).

(2) For the fixed rupture times, the slip velocities, final slips and rupture durations are functions only of the dynamic stress drop (Quin 1990). To estimate the distribution of stress drop, Miyatake (1992) proposed a method to solve directly the linear equilibrium equation with boundary conditions. The stress drop obtained in this

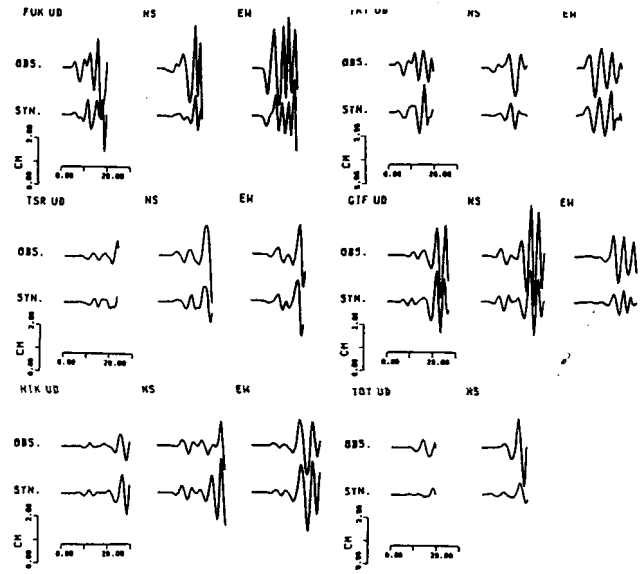

Figure 9. A comparison between the strong motion records at six stations and the corresponding synthetic seismograms obtained from the wavefrom inversion (after Takeo & Mikami 1990).

way with a constraint of non-negative values is actually local, static stress drop, assuming that the difference between static and dynamic stress drops is not significant. However, the present problem involves non-linear effects in the sense that dynamic stress drop at a single fault segment provides strong interactions between dynamic slips at adjacent segments. For this reason, we take an alternative way in this paper. We calculate dynamic rupture propagation by assigning different stress drops σ_{d_j} on each of the subdivided fault segments, and compare the resultant dynamic slip D_j^d with the slip D_j^s obtained from the kinematic waveform inversion. The square sum of the difference between D_j^s and D_j^d, i.e. $R = \sum_j (D_j^s - \alpha_j \cdot D_j^d)^2$, can be minimized by taking a ratio $\alpha_j = D_j^s / D_j^{dx}$. The ratio α_j averaged over each of the subfaults is then multiplied to the previously assigned stress drop as $\sigma_{d_j}^{(n+1)} = \alpha_j^{(n)} \cdot \sigma_{d_j}^{(n)}$, and $\alpha_j^{(n+1)}$ will then be calculated at a next stage. This iteration procedure is repeated several times until we obtain a best fit in such a way that $|R^{(n+1)} - R^{(n)}| < \delta$, where δ is set to be reasonably small.

4.3 Final dynamic model

Fig. 10 again illustrates a perspective view of the fault slips V_1' and V_2' at time steps of every 2 s, which are calculated from the final model. In contrast to the results for a uniform stress drop shown in Fig. 5, we notice a strongly heterogeneous distribution of fault slip. The slips V_1' on the hanging wall side are appreciably larger than V_2' on the foot wall side as in the initial model. The final slip reaches 108 cm for V_1' and 52 cm for V_2', respectively. The displacement source time functions calculated from the final model are also shown in Fig. 11. We see that the arrival times of rupture at points E, F and G are appreciably delayed from those for the initial model, reflecting slower rupture propagation in the final model, and that the rise times appear shortened at points A, B, C and E but extended at D.

Fig. 12 shows again the temporal pattern of dynamic rupture propagation and total fault slips $V_1' - V_2'$ given at every 1 s up to 10 s when all the rupture process was completed. As clearly noticed, the rupture propagates quite incoherently and the distribution of the fault–slip indicates an extremely heterogeneous pattern. The maximum total slip at the final stage reaches 160 cm. All these results are well matched with the results from the waveform inversion. It is found from the dynamic model that the total release of seismic moment is 7.1×10^{25} dyne · cm, which falls in between the estimates by Takeo & Mikami (1990) and Kawasaki (1975).

4.4 Distribution of dynamic stress drop and strength excess on the fault

The distribution of dynamic stress drop $\sigma_0 - \sigma_d$ and strength excess $\sigma_s - \sigma_0$ obtained from the present analysis are shown in Fig. 13(a) and (b), respectively, where these values are given in bars (×10 MPa). It can be seen that local stress drop exceeds 5 MPa in the northeastern shallower and bottom sections of the fault, 3 MPa in most of the deep section, and 4 MPa near the southwestern edge at mid-depth, as indicated by stippled zones, respectively,

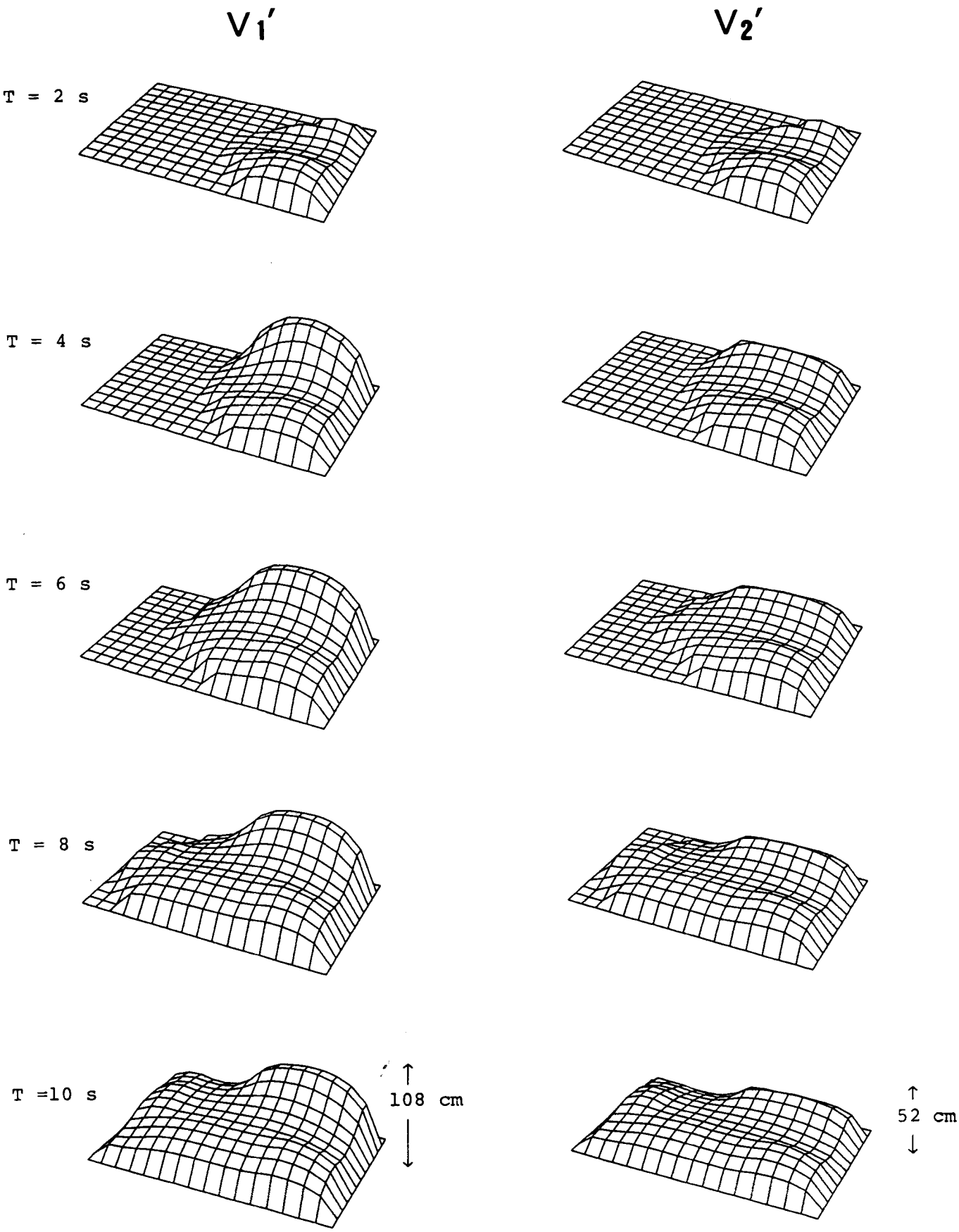

Figure 10. Temporal patterns of rupture propagation and fault slips for the final dynamic rupture model. V_1' and V_2' are the fault-slips right above and right below the fault plane, respectively.

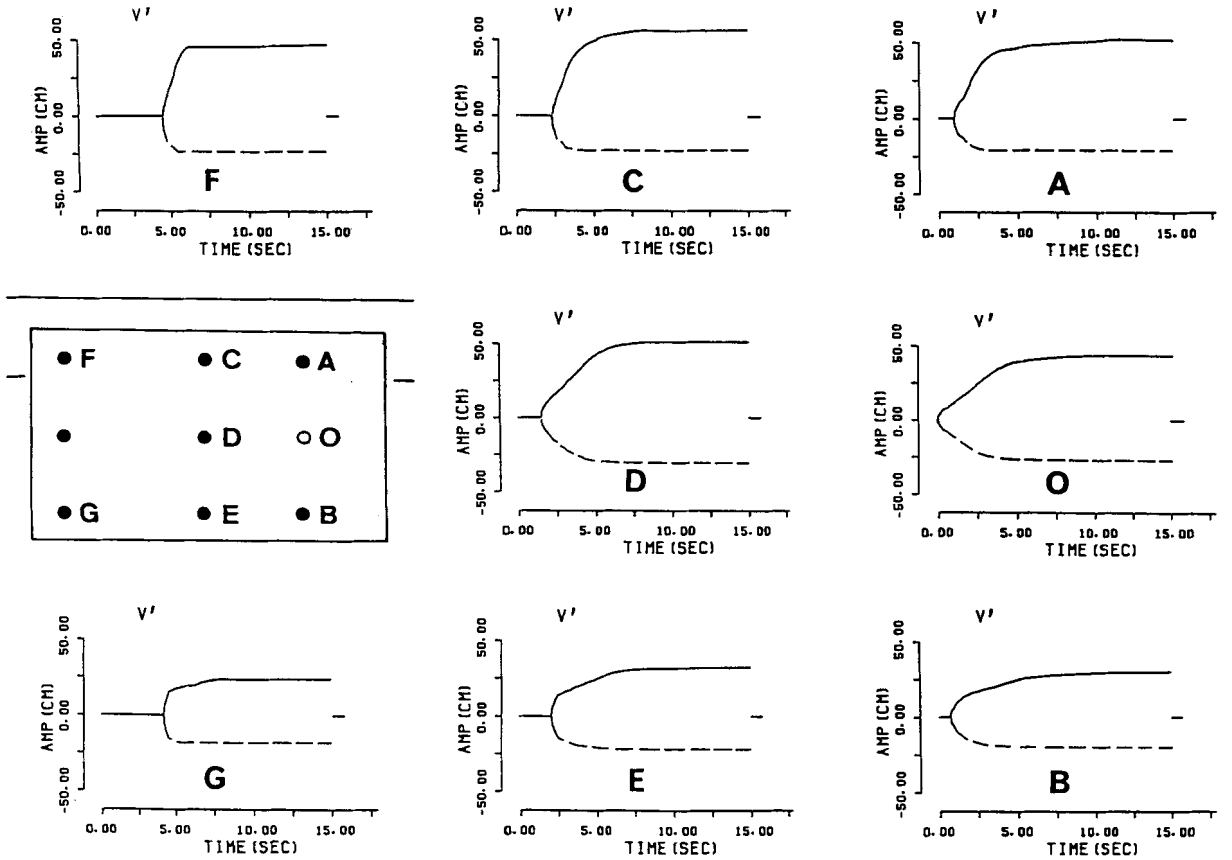

Figure 11. The displacement source time functions at the initiation point of rupture (O) and at several selected sites on the fault plane (A–G). Solid and broken curves indicate the displacement components V_1' and V_2' parallel to the fault plane.

while it is generally smaller than 2 MPa at most of the mid-depths including around the initiation point of rupture. The estimated strength excess, although it is a lower bound, shows large values exceeding 3 MPa near the southwestern edge at a shallow depth and in the central bottom section. It is noticed, however, that the strength excess is quite small at mid-depths in the northeastern triangled zone, implying that the tectonic stress had reached marginally the level of the peak shear strength in this zone. This pattern can naturally explain why the dynamic rupture started from a point in this zone or the zone became the hypocentre. However, the dynamic stress drop is not very large around its initiation point. The two different distributions suggest that the rupture started initially with a small stress drop near the nucleus zone where the tectonic stress had attained the fault strength, and that the initiation of dynamic rupture has increased the shear stress in adjacent zones, then broken the northeastern shallower and deeper fault sections with moderate strengths due to high stress drop and spread progressively southwestwards. After this time, the rupture was encountered by barriers with high strength as indicated by decelerated rupture fronts between 4 and 6 s shown in Fig. 8, and finally overcome the barriers.

Fig. 14 gives the distribution of a dimensionless stress ratio S (Das & Aki 1977a) which is defined as the ratio of the strength excess to the dynamic stress drop. For smaller S values, that is, smaller strength excess and larger stress drop, which may be regarded as the break of an asperity (Kanamori 1981), it is easier for the rupture to propagate smoothly without encountering any barriers. On the other hand, larger strength excess and smaller stress drop provide larger S values and hence stronger resistance to rupture propagation, which should be regarded as a barrier (Das & Aki 1977b; Aki 1979). In Fig. 14, S values larger than 1.0 are depicted by a stippled zone. It is interesting to note that the barrier zone extends obliquely with some breadth from the shallow-to-deep sections of the rault, and that this worked to decelerate rupture propagation as understood from Fig. 8. It should also be remarked that a number of aftershocks were concentrated near the southwestern shallow section, as shown in Fig. 15, (Takeo & Mikami 1990) where high strength excess and large S have been detected.

5 DISCUSSION

In this section, we discuss several relevant problems in some detail, on the basis of the above results.

(1) It has been postulated recently that the frictional strength or the peak shear strength σ_s increases almost linearly with depth in the brittle regime in the shallower part of the continental crust, following a friction law (Byerlee 1978), and remains nearly constant in the transition zone between the fully brittle and fully ductile regimes, while it decreases rapidly with depth in the ductile regime in the lower crust, following a steady-state creep law (e.g. Sibson

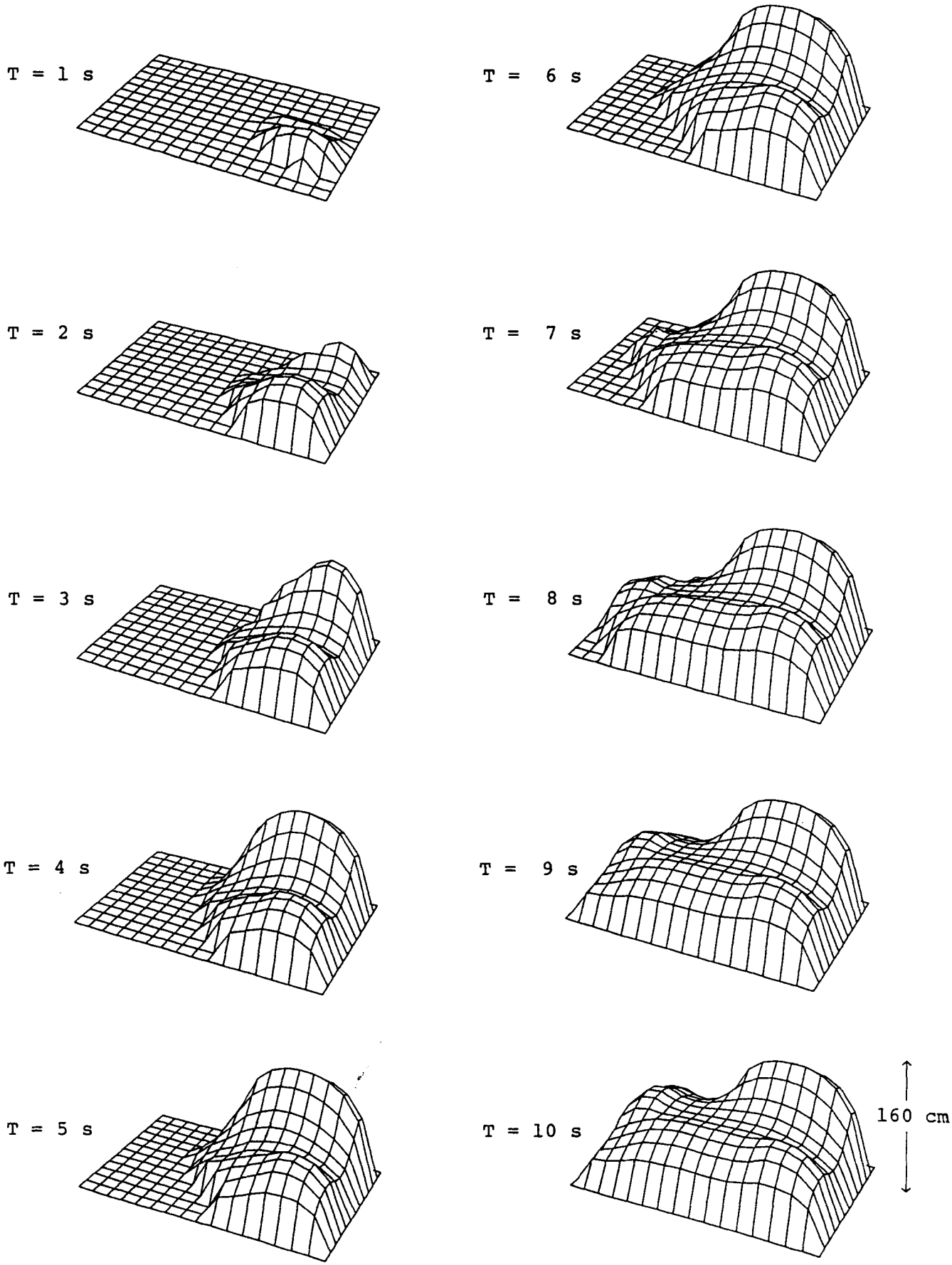

Figure 12. Temporal patterns of rupture propagation and total fault slip $V_1' - V_2'$ for the final dynamic rupture model.

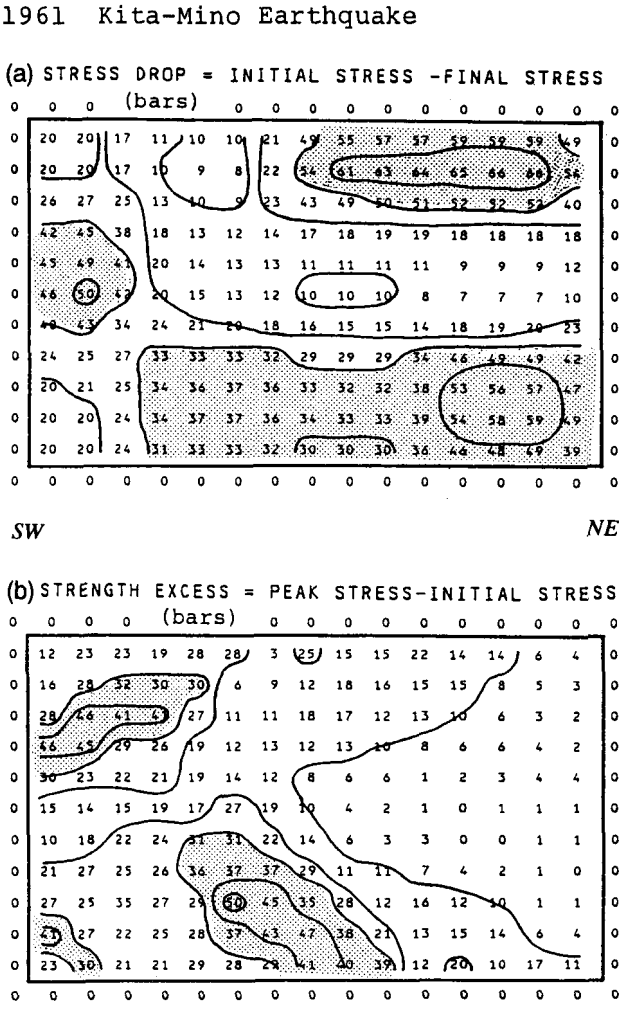

Figure 13. (a) The distribution of dynamic stress drop $\sigma_0 - \sigma_d$ on the fault. The zones of high strength excess exceeding 3 MPa are indicated by stippled zones. (b) The distribution of strength excess $\sigma_s - \sigma_0$ on the fault. The zones of high strength excess exceeding 3 MPa are indicated by stippled zones.

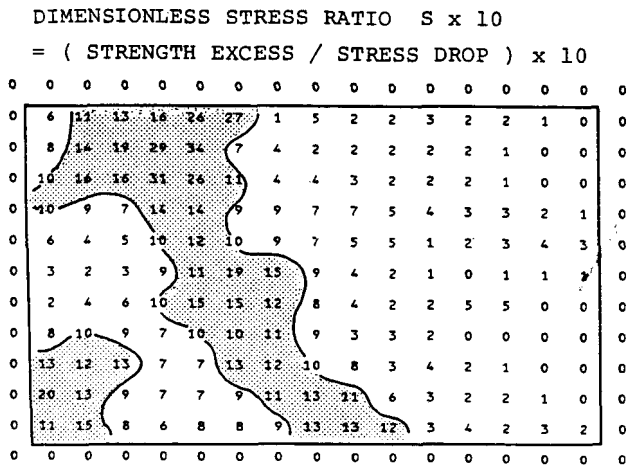

Figure 14. Distribution of the dimensionless stress ratio S which is defined as the ratio of the strength excess to the dynamic stress drop. The zones of large S values exceeding 1.0 are indicated by stipples zones.

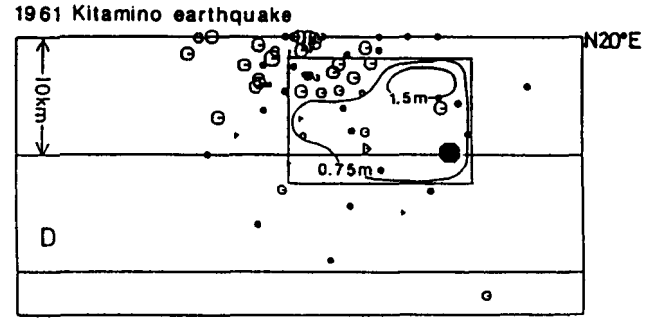

Figure 15. Distribution of aftershocks of the 1961 Kita-Mino earthquake in central Honshu, Japan (Takeo & Mikami 1990).

1984; Strehlau 1986; Ohnaka 1992; Mikumo 1992). The transition depths from the brittle to semi-brittle regimes and from the semi-brittle to the ductile regimes depend on the geothermal state within the crust. The expected dynamic stress drop $\sigma_0 - \sigma_d$ and the strength excess $\sigma_s - \sigma_0$ are also depth-dependent, and their possible depth profiles have been constructed for likely temperature distributions in the crust (Mikumo 1992). The dynamic stress drop could be negative in the semi-brittle regime below some depth with temperatures above 300–350 °C (e.g. Tse & Rice 1986), as suggested by recent laboratory experiments. In the present earthquake, we notice some depth dependence of the stress drop, with two peaks at depths around 2 and 10 km in the major part of fault sections and a lowest value around 6 km. However, no negative stress drop has been detected in this case. This distribution is different from that for the 1979 Imperial Valley, California earthquake (Quin 1990), in which the largest stress drop has been found at depths around 10 km, and negative stress drop has actually been detected at depths around 13 km and shallower than 7 km. One possible reason for the absence of negative stress drop in the present case might be due either to the coarse subfaults used in the waveform inversion or that the deeper edge of the dipping fault located at 10 km does not reach the semi-brittle zone.

The depth dependence of the strength excess in the present earthquake is rather weak, and its lateral variations are more dominant, as in the case of Japanese inland earthquakes (Fukuyama & Mikumo 1992; Miyatake, in preparation). For the Imperial Valley earthquake, however, some dependence has been found with larger values at depths between 5 and 13 km (Quin 1990).

(2) The strength excess estimated here depends on the grid spacing used in the numerical calculations as mentioned before, since it has been calculated from the peak shear stress at the rupture front just before the relevant fault segment breaks. It has now been widely accepted that there should be a cohesive zone or breakdown zone just ahead of the propagating crack tip. The size of the breakdown zone has been estimated from seismic energy consideration to be a few hundred metres for moderate-size earthquakes (Aki 1992). Basically, it is necessary to estimate the peak stress ahead of the breakdown zone, but the grid spacing used here is 1 km, which is not fine enough to resolve a breakdown zone. However, we might be able to estimate the absolute value of the peak stress in the following way. Since the average stress over the grids immediately outside

the crack tip is inversely proportional to the square root of the grid spacing (Aki & Richards 1980), a realistic maximum shear stress at the rupture front or the strength excess would be of the order of 1.4–1.7 times the present estimate if the possible size of the breakdown zone is 300–500 m as compared with the grid spacing of 1 km used here.

(3) Although the distribution of the slip velocity for the final model is not explicitly shown, the initial slip velocity may be estimated from the fault–slip and rise time such as shown in Fig. 11. These values estimated at 8 points, A, O, B, C, D, E, F and G are, 152/2.0, 78/5.0, 72/1.5, 127/2.0, 69/3.5, 65/1.8, 80/1.8 and 48/1.5 cm s^{-1}, where the numerators and denominators are the fault slip $V_1' - V_2'$ and the rise time, respectively. It should be mentioned that the rise times obtained from the present dynamic rupture model ranges from about 1.5 to 3.5 s depending on the location on the fault plane, except at the initiation point of rupture (O). The rise times and slip velocities may well be compared with those from kinematic dislocation models to match the synthetic waveforms with the corresponding strong motion records. It has been noticed for long years (e.g. Bouchon 1978) and explicitly pointed out recently (Heaton 1990) that the rise times estimated from the modelling of strong motion data are significantly shorter than those calculated from 2- and 3-D crack models, and that the crack models without barriers could not provide rise times to be compared with seismic waveforms. This is indeed the case if the fault has a relatively uniform strength and hence if the rupture propagates with a constant speed. Heaton (1990) introduced a self-healing model with a simple rate-dependent friction law in order to reconcile the above discrepancy. This healing mechanism could be one of possible models. Our results show, however, that the dynamic rupture model with the existence of a few barriers of high strength excess could also account for the shorter rise times to considerable extent.

The present results indicate that the dimension of barrier zones detected here is of the order of several kilometres which corresponds to 25 to 45 per cent of the fault dimension. The relatively large size of the barrier zones may come from the seismic-wave frequency and the size of the subfaults dealt with in the waveform inversion. It should be emphasized here that the fault zone of the present earthquake involves not only the barriers but also a few large-scale asperities at the same time.

CONCLUSIONS

We have investigated the dynamic rupture processes on a dipping fault embedded in a horizontally layered medium, as a spontaneous, dynamic shear crack in a 3-D space. The displacement components right above and right below the dipping fault have been obtained by solving the boundary conditions across the fault. The results indicate that the final fault–slips on the hanging wall side are appreciably larger than those on the foot wall side, and that these are quite sensitive to the depth to the dipping fault as well as to heterogeneous elastic properties of the medium, particularly of the existence of low-velocity surface layers.

On the basis of the above model, the dynamic rupture process of the 1961 Kita–Mino earthquake that occurred in central Honshu, Japan, has been investigated in detail, with constraints of the fault parameters derived from the results of kinematic waveform inversion of strong motion data (Takeo & Mikami 1990). From the rupture times obtained from the kinematic waveform inversion, a lower bound of the peak shear stress and hence of the strength excess has been estimated. The dynamic stress drop has also been calculated through repeated iterations so as to minimize the difference between the resultant dynamic kinematic and fault slips. It was found that the distribution of the local stress drop is quite heterogeneous, exceeding 5 MPa in the northeastern shallow and bottom sections of the fault, and 4 MPa near the southwestern edge at mid-depth, while it is generally smaller than 2 MPa at most of the mid-depth. The strength excess also shows large lateral variations, with large values near the southwestern edge at shallow depths and in the central deep section, in contrast to small values at mid-depths over the northeastern section including the nucleus zone of rupture.

These results indicate that the dynamic rupture initiated at a small zone with low strength excess and low stress drop, then broke the northeastern shallower and deeper sections with moderate-strength excess and high stress drop, and was encountered by barrier zones with high-strength excess, decelerating rutpure propagation. These zones may be interpreted as weak and strong asperities, and barriers, respectively, as also indicated by a dimensionless stress ratio S. The size of the barrier zones is of the order of several kilometres. The above dynamic process yielded the rise times ranging between 1.5 and 3.5 s that could satisfy the results from the inversion results.

ACKNOWLEDGMENTS

We wish to thank Drs N. Mikami and M. Takeo for allowing us to use their results from inversion analysis for our present study. The computations involved here were made at the Data Processing Center of Kyoto University.

REFERENCES

Aki, K., 1979. Characterization of barriers on an earthquake fault, *J. geophys. Res.*, **84** 6140–84 6148.

Aki, K., 1992. Higher order interrelations between seismogenic structures and earthquake processes, *Tectonophysics*, **211**, 1–12.

Aki, K. & Richards, P. G., 1980. *Quantitative Seismology: Theory and Methods*, W. H. Freeman, San Francisco.

Andrews, D. J., 1976. Rupture velocity of plane strain shear cracks, *J. geophys. Res.*, **81**, 5679–5687.

Beroza, G. C. & Spudich, P., 1988. Linearized inversion for fault rupture behavior: application to the 1984, Morgan Hill, California, earthquake, *J. geophys. Res.*, **93**, 6275–6296.

Bouchon, M., 1978. A dynamic source model for the San Fernando earthquake, *Bull. seism. Soc. Am.*, **68**, 1555–1576.

Byerlee, J. D., 1978. Friction of rocks, *Pure appl. Geophys.*, **116**, 615–526.

Das, S., 1981. Three-dimensional spontaneous rupture propagation and implication for the earthquake source mechanism, *Geophys. J. R. astr. Soc.*, **67**, 375–393.

Das, S. & Aki, K., 1977a. A numerical study of two-dimensional spontaneous rupture propagation, *Geophys. J. R. astr. Soc.*, **50**, 643–668.

Das, S. & Aki, K., 1977b. Fault plane with barriers: A versatile earthquake model, *J. geophys. Res.*, **82**, 5658–5670.

Day, S. M., 1982. Three-dimensional simulation of spontaneous

rupture: The effect of nonuniform prestress, *Bull. seism. Soc. Am.*, **72,** 1881–1902.

Dieterich, J. H., 1981. Constitutive properties of faults with simulated gouge in mechanical behavior of crustal rocks, in *Geophys. Monogr, Ser.* 24, pp. 103–120, eds Carter, N. L., Friedman, M., Logan, J. M. & Stearns, D. W., Am. Geophys. Un.

Fukuyama, E., 1991a. Analysis and interpretation of the heterogeneous rupture process: application of the empirical Green's function method and nonlinear inversion technique to large earthquakes, *Tectonophysics,* **197,** 1–17.

Fukuyama, E., 1991b. Inversion for the rupture details of the 1987 east Chiba earthquake, Japan, using a fault model based on the distribution of relocated aftershocks, *J. geophys. Res.*, **96,** 8205–8217.

Fukuyama, E. & Irikura, K., 1986. Rupture process of the 1983 Japan Sea (Akita–Oki) earthquake using a waveform inversion method, *Bull. seism. Soc. Am.*, **76,** 1623–1649.

Fukuyama, E. & Mikumo, T., 1992. Dynamic rupture analysis: Inversion for the source process of the 1990 Izu–Oshima, Japan earthquake (M6.5), *J. geophys. Res,* in press.

Hamada, N., 1984. Re-examination of aftershock distribution and seismic activity associated with inland earthquakes, Japan, *Prog. Abstr. seism. Soc. Japan,* **1,** 75 (in Japanese).

Hartzel, S. & Heaton, T. H., 1983. Inversion of strong ground motion and teleseismic waveform data for the fault rupture history of the 1979 Imperial Valley, California earthquake, *Bull. seism. Soc. Am.*, **73,** 1553–1583.

Heaton, T. H., 1990. Evidence for the implications of self-healing pulses of slip in earthquake rupture, *Phys. Earth planet. Interiors,* **64,** 1–20.

Kanamori, H. 1981. The nature of seismicity pattern before large earthquakes, in *Earthquake Prediction—an International Review,* pp. 1–19., Maurice Ewing Series 4, Am. Geophys. Un.

Kawasaki, I., 1975. The focal process of the Kita–Mino earthquake of August 1961, and its relationship to a quaternary fault, the Hatogau-Koike fault, *J. Phys. Earth,* **23,** 145–159.

Kikuchi, M. & Kanamori, H., 1982. Inversion of complex body waves, *Bull. seism. Soc. Am.*, **72,** 491–506.

Levander, A. R., 1985. Use of the telegraphy equation to improve absorbing boundary efficiency for fourth-order acoustic wave finite difference scheme, *Bull. seism. Soc. Am.*, **75,** 1847–1825.

Mikumo, T., 1992. Dynamic fault rupture and stress recovery processes in continental crust under depth-dependent shear strength and frictional parameters, *Tectonophysics,* **211,** 201–222.

Mikumo, T. & Miyatake, T., 1978. Dynamical rupture process on a three-dimensional fault with non-uniform frictions and near-field seismic waves, *Geophys. J. R. astr. Soc.*, **54,** 417–438.

Mikumo, T. & Miyatake, T., 1979. Earthquake sequences on a frictional fault model with non-uniform strength and relaxation times, *Geophys. J. R. astr. Soc.*, **59,** 497–522.

Mikumo, T., Hirahara, K. & Miyatake, T., 1987. Dynamical fault rupture processes in heterogeneous media, *Tectonophysics,* **144,** 19–36.

Miyatake, T., 1980. Numerical simulations of earthquake source process by a three-dimensional crack model. Part I. Rupture process. *J. Phys. Earth,* **28,** 565–598.

Miyatake, T., 1992. Reconstruction of dynamic rupture process of an earthquake with constraints of kinematic parameters, *Geophys. Res. Lett.*, **19,** 349–352.

Ohnaka, M., 1992. Earthquake source nucleation: a physical model for short-term precursors, *Tectonophysics,* **211,** 149–178.

Olson, A. H. & Apsel, R., 1982. Finite faults and inverse theory with applications to the 1979 Imperial Valley earthquake, *Bull. Seism. Soc. Am.*, **72,** 1969–2002.

Quin, H., 1990. Dynamic stress drop and rupture dynamics of the October 15, 1979 Imperial Valley, California, earthquake, *Tectonophysics,* **175,** 93–117.

Ruina, A. L., 1983. Slip instability and state variable friction laws, *J. geophys. Res.*, **88,** 10 359–10 370.

Sibson, R. H., 1984. Roughness at the base of the seismogenic zone: contributing factors, *J. geophys. res.*, **89,** 5791–5799.

Spudich, P. & Frazier, L. N., 1984. Use of ray theory to calculate high-frequency radiation from earthquake sources having spatially variable rupture velocity and stress drop, *Bull. seism. Soc. Am.*, **74,** 2061–2082.

Strehlau, J., 1986. A discussion of the depth extent of rupture in large continental earthquakes, in *Earthquake Source Mechanics,* pp. 131–145, eds Das, S., Boatwright, J. & Scholz, C. H., Geophys. Monogr. Ser., Am. Geophys. Un.

Takeo, M., 1987. An inversion method to analyze the rupture process of earthquakes using near-field seismograms, *Bull. seism. Soc. Am.*, **77,** 490–513.

Takeo, M., 1988. Rupture process of the 1980 Izu–Hanto–Oki earthquake deduced from strong motion seismograms, *Bull. seism. Soc. Am.*, **78,** 1074–1091.

Takeo, M. & Mikami, N., 1987. Inversion of strong motion seismograms for the source process of the Nagano–Ken–Seibu earthquake of 1984, *Tectonophysics,* **144,** 271–285.

Takeo, M. & Mikami, N., 1990. Fault heterogeneity of inland earthquakes in Japan, *Bull. Earthq. Res. Inst.*, **65,** 541–569.

Toki, K. & Sawada, S., 1988. Simulation of the fault rupture process and near-field ground motion by the three-dimensional finite element method, *Proc. 9th CWEE,* Tokyo, Vol. **2,** 751–756.

Tse, S. T. & Rice, J. R., 1986. Crustal earthquake instability in relation to the depth variation of frictional slip properties, *J. geophys. Res.*, **91,** 9452–9472.

Virieux, J. & Madariaga, R., 1982. Dynamic faulting studied by a finite difference method, *Bull seism. Soc. Am.*, **72,** 345–369.

Yamashita, T., 1976. On the dynamical process of fault motion in the presence of friction and homogeneous initial stress, Part II. Rupture propagation, *J. Phys. Earth,* **24,** 417–444.

Yomogida, K., 1988. Crack-like rupture processes observed in near-fault strong motion data, *Geophys. Res. Lett.*, **15,** 1223–1226.

APPENDIX

We describe here the boundary conditions on the fault plane [eq. (3) in the text] in some detail. Since the fault plane is inclined with a dip of θ with respect to the free surface, the stress components in equation (1) referring to the $x'y'z'$ coordinate system can be transformed into the following way,

$$\sigma_{y'z'} = \sigma_{yy}\sin\theta\cos\theta - \sigma_{zz}\sin\theta\cos\theta - (\cos^2\theta - \sin^2\theta)\sigma_{yz}$$
$$= \mu\left[\left(\frac{\partial v}{\partial y} - \frac{\partial w}{\partial z}\right)\sin 2\theta - \left(\frac{\partial w}{\partial y} + \frac{\partial v}{\partial z}\right)\cos 2\theta\right].$$

$$\sigma_{z'x'} = -\sigma_{zx}\sin\theta - \sigma_{xy}\cos\theta$$
$$= -\mu\left[\left(\frac{\partial u}{\partial z} + \frac{\partial w}{\partial y}\right)\sin\theta + \left(\frac{\partial u}{\partial y} + \frac{\partial v}{\partial z}\right)\cos\theta\right] \qquad \text{(A1)}$$

$$\sigma_{z'z'} = \sigma_{zz}\sin^2\theta + \sigma_{yy}\cos^2\theta + 2\sigma_{yz}\sin\theta\cos\theta$$
$$= \lambda\left(\frac{\partial u}{\partial x} + \frac{\partial v}{\partial y} + \frac{\partial w}{\partial z}\right) + 2\mu\left(\frac{\partial v}{\partial y}\cos^2\theta + \frac{\partial w}{\partial z}\sin^2\theta\right)$$
$$+ \mu\left(\frac{\partial v}{\partial z} + \frac{\partial w}{\partial y}\right)\sin 2\theta.$$

If the space derivatives included in eq. (A1) are replaced by the finite difference in the respective

displacement components, eqs 3 (a), (b), (c) and (d) in the text can be expressed in the following forms, respectively,

$$\begin{aligned} &AV_1 + BW_1 = E_1 + S. && \text{(a)}\\ &-AV_2 - BW_2 = E_2 - S. && \text{(b)}\\ &CV_1 + DW_1 + F_1 = -CV_2 - DW_2 + F_2. && \text{(c)}\\ &PV_1 + QW_1 = PV_2 + QW_2. && \text{(d)}\\ &V_1 \equiv v_1(i, j, k), \qquad W_1 \equiv w_1(i, j, k)\\ &V_2 \equiv v_2(i, j, k), \qquad W_2 \equiv w_2(i, j, k). \end{aligned} \tag{A2}$$

where subscripts i, j and k are index numbers of the discretized grid points in the x-, y- and z-directions, respectively. Since the points (i, j, k) are located on the dipping fault plane, j and k are related with each other as $k = k0 - j + 1$, $k0$ being the point on the ground surface encountered by the dipping plane. All the above quantities and coefficients included in Eq. (A2) can be explicitly written as,

$$\begin{aligned} S &= \sigma_0 - \sigma_d\\ A &= -\mu(\sin 2\theta/\Delta y - \cos 2\theta/\Delta z)\\ B &= \mu(\sin 2\theta/\Delta z + \cos 2\theta/\Delta y)\\ E_1 &= -\mu \sin 2\theta \cdot v_1(i, j-1, k)/\Delta y\\ &\quad + \mu \cos 2\theta \cdot v_1(i, j, k-1)/\Delta z\\ &\quad + \mu \sin 2\theta \cdot w_1(i, j, k-1)/\Delta z\\ &\quad + \mu \cos 2\theta \cdot w_1(i, j-1, k)/\Delta y\\ E_2 &= -\mu \sin 2\theta \cdot v_2(i, j+1, k)/\Delta y\\ &\quad + \mu \cos 2\theta \cdot v_2(i, j, k+1)/\Delta z\\ &\quad + \mu \sin 2\theta \cdot w_2(i, j, k+1)/\Delta z\\ &\quad + \mu \cos 2\theta \cdot w_2(i, j+1, k)/\Delta y\\ C &= -(\lambda + 2\mu \cos^2\theta)/\Delta y - \mu \sin 2\theta/\Delta z\\ D &= -(\lambda + 2\mu \sin^2\theta)/\Delta z - \mu \sin 2\theta/\Delta y\\ F_1 &= (\lambda + 2\mu \cos^2\theta) \cdot v_1(i, j-1, k)/\Delta y\\ &\quad + \mu \sin 2\theta \cdot v_1(i, j, k-1)/\Delta z\\ &\quad + (\lambda + 2\mu \sin^2\theta) \cdot w_1(i, j, k-1)/\Delta z\\ &\quad + \mu \sin 2\theta \cdot w_1(i, j-1, k)/\Delta y\\ F_2 &= (\lambda + 2\mu \cos^2\theta) \cdot v_2(i, j+1, k)/\Delta y\\ &\quad + \mu \sin 2\theta \cdot v_2(i, j, k+1)/\Delta z\\ &\quad + (\lambda + 2\mu \sin^2\theta) \cdot w_2(i, j, k+1)/\Delta z\\ &\quad + \mu \sin 2\theta \cdot w_2(i, j+1, k)/\Delta y\\ P &= \cos\theta, \quad Q = \sin\theta. \end{aligned}$$

The four displacement components can be solved from eq. (A2) through some algebraic calculations,

$$\begin{aligned} &V_1 = (N_1 + M_1)/2, \qquad V_2 = (N_1 - M_1)/2\\ &W_1 = (N_2 + M_2)/2, \qquad W_2 = (N_2 - M_2)/2 \end{aligned} \tag{A3}$$

where

$$\begin{aligned} M_1 &= -Q(2S + E_1 - E_2)/(BP - AQ)\\ M_2 &= P(2S + E_1 - E_2)/(BP - AQ)\\ N_1 &= -[B(F_1 + F_2) + D(E_1 + E_2)]/(BC - AD)\\ N_2 &= [A(F_1 + F_2) + C(E_1 + E_2)]/(BC - AD), \end{aligned}$$

and

$$\begin{aligned} &V_1' = -QV_1 + PW_1, \qquad V_2' = -QV_2 + PW_2\\ &W_1' = W_2' = -(PN_1 + QN_2)/2. \end{aligned} \tag{A4}$$

Combining eq. 3 (e) and $u_1(i, j, k) = u_2(i, j, k) \equiv U$, we obtain,

$$\begin{aligned} R \cdot U &= [u_1(i, j, k-1) + u_2(i, j, k+1)] \sin\theta/\Delta z\\ &\quad + [u_1(i, j-1, k) + u_2(i, j+1, k)] \cos\theta/\Delta y\\ &\quad + [v_2(i-1, j, k) - v_2(i+1, j, k)] \cos\theta/2\Delta x\\ &\quad + [v_1(i-1, j, k) - v_1(i+1, j, k)] \cos\theta/2\Delta x\\ &\quad + [w_2(i-1, j, k) - w_2(i+1, j, k)] \sin\theta/2\Delta x\\ &\quad + [w_1(i-1, j, k) - w_1(i+1, j, k)] \sin\theta/2\Delta x \end{aligned} \tag{A5}$$

where

$R = 2(\sin\theta/\Delta z + \cos\theta/\Delta y)$.

For the fault segments that have not yet been broken or on the plane extended from the fault, we have the boundary conditions analogous to eq. (3),

$$\begin{aligned} &(\sigma_{y'z'})_1 = (\sigma_{y'z'})_2 && \text{(a)}\\ &(\sigma_{z'z'})_1 = (\sigma_{z'z'})_2 && \text{(b)}\\ &v_1' = v_2' && \text{(c)}\\ &w_1' = w_2'. && \text{(d)} \end{aligned} \tag{A6}$$

Eq. A6 (a) has the same form as in eqs 3 (a) and (b) without stress drop, and eq. A6 (c) holds in this case since there is no displacement discontinuity across the plane at this moment. Eqs A6 (a) and (c) can be written as,

$$\begin{aligned} &AV_1 + BW_1 - E_1 = -AV_2 - BW_2 + E_2 && \text{(a)}\\ &-QV_1 + PW_1 \quad = -QV_2 + PW_2. && \text{(c)} \end{aligned} \tag{A7}$$

Combining eqs A7 (a) and (c) with eqs A2 (c) and (d), we obtain,

$$V_1 = V_2 = N_1/2, \qquad W_1 = W_2 = N_2/2. \tag{A8}$$

Thus, we can calculate the displacement components right above and right below the fault plane by using the boundary conditions, as illustrated in Fig. 2, since the displacements at points $(i, j-1, k)$, $(i, j, k-1)$, $(i, j+1, k)$ and $(i, j, k+1)$ are obtained by solving the wave equation.

For grid points on the ground surface, we obtain the displacement components from the free surface boundary conditions. For two special points close to the upper side of the dipping plane, i.e. for $k = k0 - 1$ and $k = k0$, we have,

$$\begin{aligned} v_1(i, 1, k) &= v_1(i, 1, k-1) + (\Delta z/\Delta y)[w_1(i, 1, k-1)\\ &\quad - w_1(i, 2, k-1)]\\ w_1(i, 1, k) &= w_1(i, 1, k-1) + (\Delta z/\Delta y)[v_1(i, 1, k-1)\\ &\quad - v_1(i, 2, k-1)]/(\lambda + 2\mu)/\lambda\\ &\quad + (\Delta z/2\Delta x)[u_1(i+1, 1, k) - u_1(i-1, 1, k)]. \end{aligned} \tag{A9}$$

It is also necessary to calculate fictitious displacements at point $(i, j-1, k)$ for $j-1$ above the ground surface, in order to obtain E_1 and F_1.

$$\begin{aligned} v_1(i, 0, k0) &= v_1(i, 1, k0) + (\Delta y/\Delta z)[w_1(i, 1, k0-1)\\ &\quad - w_1(i, 1, k0-2)]\lambda/\lambda + 2\mu)\\ w_1(i, 0, k0) &= w_1(i, 1, k0)\\ &\quad + (\Delta y/\Delta z)[v_1(i, 1, k0-1) - v_1(i, 1, k0-2)]. \end{aligned} \tag{A10}$$